Computational Materials Science II

Progress Report # 2

Vourvachakis S. Georgios
mse354

March 24, 2025

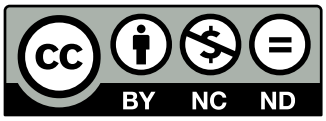

Contents

1

Introduction

The properties of a material's surface often differ substantially from those of its bulk, with implications for catalysis, adhesion, electronic behavior, and more. Density Functional Theory (DFT) simulations provide a robust framework for understanding these differences. In particular, GPAW—a real-space, projector augmented-wave (PAW) code—has proven effective for modeling surface phenomena and exploring how cutting an infinite crystal into slabs affects the total energy and structure.[Jai+13],[Cha+21], [Mer+23]

1.1 From Bulk to Surface

Consider an infinite crystal that is partitioned into slabs. Each slab is modeled as infinite in two dimensions (with area A) and finite in the third (thickness w), with a vacuum region of width v inserted between slabs. When both w and v are much larger than the lattice constant, one can show that the energy of a slab is given by

$$E = NE_{\text{bulk}} + 2\gamma A\,,$$

where N is the number of atoms in the slab, E_{bulk} is the energy per atom in the bulk, and γ is the surface energy (or surface tension, with units of energy per unit area). The proof follows by noting that in an ideal bulk crystal each atom contributes E_{bulk}. When the crystal is cleaved to create surfaces, bonds are broken at the interface, leading to an additional energy penalty that is proportional to the area of the new surfaces. Since there are two surfaces in a symmetric slab, the extra energy is $2\gamma A$.[FM96]

1.2 Crystallographic Orientation and Miller Indices

The atomic arrangement at a surface depends critically on the crystallographic orientation. In crystalline materials, the orientation of a plane is defined by Miller indices (hkl). For a cubic crystal, the plane (hkl) is perpendicular to the direct-lattice vector $\mathbf{r}_{hkl} \coloneqq h\hat{\mathbf{x}} + k\hat{\mathbf{y}} + l\hat{\mathbf{z}}$, this vector corresponds to the reciprocal-lattice vector $\mathbf{g}_{hkl} \coloneqq h\mathbf{b}_1 + k\mathbf{b}_2 + l\mathbf{b}_3$, where $\mathbf{b}_i$ are the primitive reciprocal-lattice vectors. The Miller indices thus encode the periodicity and symmetry of the crystal surface, directly determining the atomic arrangement at the surface termination.[SS11]

In surface science, the orientation of a plane (hkl) dictates:

1. **Surface Atomic Density**: Planes with higher Miller indices (e.g., (110) vs. (100) in cubic systems) often exhibit lower atomic packing, leading to higher surface energies due to under-coordinated atoms.
2. **Termination Symmetry**: For example, the (111) face of an FCC metal (e.g., Au) has a hexagonal close-packed arrangement, while (100) is square-symmetrical.

3. **Relaxation and Reconstruction**: Surfaces may undergo atomic displacements (relaxation) or structural rearrangements (reconstruction) to minimize energy, as observed in LEED experiments[VT12] (e.g., the infamous (7×7) reconstruction of Si(111)[Bin+83]).

1.2.1 Surface Energy and Orientation Dependence

The atomic arrangement at a surface, governed by its (hkl) orientation, critically influences its surface energy ($\gamma_{(hkl)}$). Moritz and Van Hove highlight that surfaces with higher atomic coordination (e.g., densely packed (111) in FCC metals) typically exhibit lower $\gamma_{(hkl)}$ due to reduced bond-breaking penalties. Conversely, open surfaces (e.g., (211)) often have higher energies due to under-coordinated atoms and dangling bonds.[MV22]

Specifically, the number of *broken bonds per surface atom* increases with surface roughness (e.g., stepped surfaces like (211) vs. flat (111)), surface atoms may relax inward or outward to optimize bonding, as quantified by LEED I-V (intensity-voltage) analysis[GS02]. For instance, the first interlayer spacing of Al(110) contracts by ~10% compared to the bulk [HB71], and *charge density smoothing* at surfaces, observed in X-ray diffraction, lowers energy but depends on the orientation-specific electronic structure [Ing90].

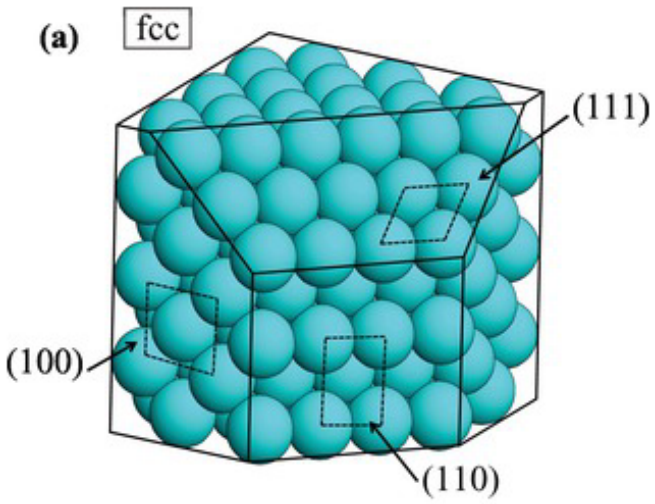

Figure 1: Low-index faces of FCC with unit cells outlined using dashed lines, which is studied in this assignment.[MV22]

1.3 The Dangling Bond Model for Surface Energy

A particularly intuitive model to estimate surface energies is the *Dangling Bond Model* (DBM) [Lan90]. In the bulk, an atom is typically coordinated by z_b nearest neighbors, and the energy associated with each bond can be approximated as

$$E_b \approx \frac{E_{at}}{z_b},$$

where E_{at} is the atomization energy—that is, the energy required to disassemble the solid into isolated atoms (which can be derived from the enthalpy of atomization)[RP13]. When a surface is created, the atoms at the surface lose some of their coordination; if a surface atom retains only z bonds (with $z < z_b$), it has $N_{db} = z_b - z$ dangling bonds. Assuming that the additional energy per dangling bond is approximately E_b, one can estimate the surface energy as

$$\gamma \approx \frac{N_{db} E_b}{A},$$

where A is the surface area associated with one atom, with N_{db} varying according to the local coordination dictated by the Miller indices. This simple picture provides reasonable estimates for different surfaces. For example, when comparing various low-index aluminum surfaces such as Al(100), Al(110), Al(111), and Al(211), we will use this estimator in our experiments.

Moreover, the standard method for calculating the surface energy is to evaluate the total energy of a slab of the material of interest (generally with a thickness between 5 to 15 layers) and to subtract from that the bulk energy obtained from a separate calculation. This procedure singles out the total energy contribution due to the presence of the surface. It is based on the general and intuitively appealing expression

$$\gamma_\infty = \frac{1}{2} \lim_{n\to\infty} \left(E^n_{\text{slab}} - n E_{\text{bulk}} \right),$$

with E^n_{slab} the total energy of an n-layer slab; the limit is approximated in practice by the nth term. The factor of 1/2 accounts for the two surfaces of the slab. However, as Boettger et al. [Boe94] pointed out, any difference between E_{bulk} and the change in E_{slab} with slab thickness will cause the calculated surface energy to diverge linearly with n. Thus, increasing the slab thickness must sooner or later lead to unacceptable results, because the bulk energy from a separate calculation will never exactly equal the slope of the slab energy versus n.

1.4 DFT Implications on Surface Statistics

The surface energy of a crystal facet (hkl) is calculated using a *slab model*. This model begins by reorienting the conventional unit cell of the bulk crystal into an *oriented unit cell* aligned with the (hkl) plane. The lattice vectors $\mathbf{a}_{\text{orient}}$ and $\mathbf{b}_{\text{orient}}$ are chosen to lie parallel to the (hkl) plane, while $\mathbf{c}_{\text{orient}}$ is oriented as close to perpendicular to the plane as possible. This alignment ensures that the surface of interest is properly exposed. Atoms within the oriented unit cell are then shifted along $\mathbf{c}_{\text{orient}}$ to generate all symmetrically distinct terminations (σ), which represent different atomic configurations at the surface due to crystal symmetry. A super-cell is constructed by repeating the oriented unit cell along $\mathbf{c}_{\text{orient}}$, followed by truncation to create a finite slab. A vacuum layer (typically $\geq$ 15 Å) is introduced to isolate periodic images of the slab. This workflow can be implemented algorithmically in the pymatgen library[Ong+13].

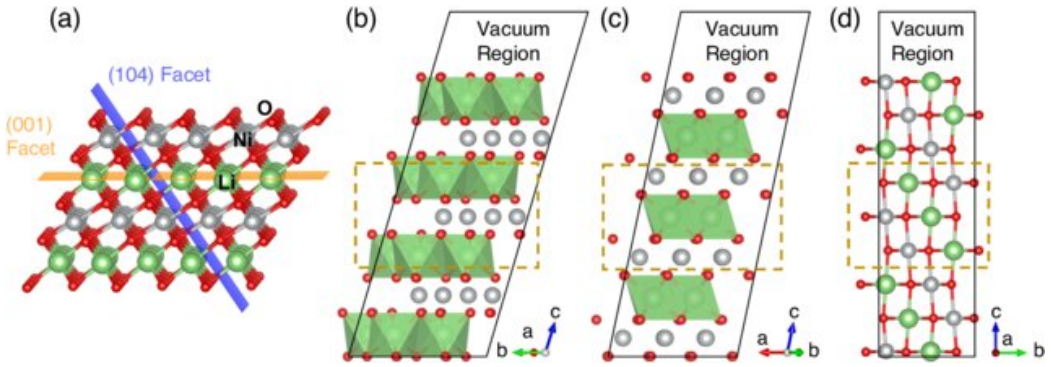

Figure 2: An example visualizations of surface slab model in practice. (a) Section of the layered $LiNiO_2$ structure highlighting the two surface facets, (001) and (104). Periodic surface slab models of the (b) Li-terminated and (c) Ni-terminated $LiNiO_2$(001) facet as well as the (d) non-polar (104) facet. The vacuum region of 15 Å is truncated in the figures. Atomic planes that are held fixed at the ideal bulk sites are indicated with orange dashed rectangles, the remaining atoms are allowed to relax. Li, Ni, and O atoms are shown in green, gray, and red, respectively.[CL13]

The surface energy $\gamma^{\sigma}_{(hkl)}$, in this framework, for termination σ is computed using the formula:

$$\gamma^{\sigma}_{(hkl)} = \left.\frac{E^{\sigma}_{\text{slab}} - N E_{\text{bulk}}}{2A_{\text{slab}}}\right|_{(hkl)}.$$

Here, $E^{(hkl),\sigma}_{\text{slab}}$ is the total energy of the relaxed slab, $E^{(hkl)}_{\text{bulk}}$ is the per-atom energy of the relaxed bulk oriented unit cell (where both atomic positions and cell volume are optimized), N is the number of atoms in the slab, and $A^{(hkl)}_{\text{slab}}$ is the cross-sectional area of the slab parallel to the (hkl) plane. Critically, the slab model relaxes only atomic positions, whereas the bulk oriented unit cell relaxes both atomic positions and volume.

All density functional theory (DFT) calculations are performed using the Grid-based Projector-Augmented Wave (GPAW) package. The projector augmented wave (PAW) method is employed for pseudo-potentials, and the Perdew-Berke-Ernzerhof (PBE) [ES99] generalized gradient approximation (GGA) models exchange-correlation effects for the case of Palladium (transition metal), and the Local Density Approximation was performed for the simpler Aluminum poor-transition metal. Spin polarization is included in the case of Palladium, with a plane-wave cutoff energy of 300 eV. A Monkhorst-Pack k-point sampling grid is used [Wan+21], dependent on the surface orientation, with coarse grid spacing of 0.25Å. Ionic relaxation proceeds until residual forces on atoms are below $0.1eV/$Å under the BFGS optimization method [XBN19]. We invoked the eq.1.4 for the DFT-based surface energy estimate.

1.5 A Framework for Equilibrium Shape

The equilibrium shape of a material is determined by minimizing its total free energy, which includes both a bulk term and a surface term. In the continuous formulation, for a region Ω with fixed volume V_0 and surface

$\partial\Omega$, the total free energy is written as

$$F[\Omega] \coloneqq G_{\text{bulk}}(V) + \int_{\partial\Omega} \gamma(\mathbf{n})\, dA\,, \text{ subject to } V = V_{\text{o}}\,.$$

Here, $G_{\text{bulk}}(V)$ is the bulk Gibbs free energy, $\gamma(\mathbf{n})$ is the orientation-dependent surface energy density (with $\mathbf{n}$ denoting the surface normal), and dA represents an infinitesimal area element.

For crystalline solids where the surface energy depends on the crystallographic orientation, the free energy is often expressed in a discrete form over individual facets labeled by their Miller indices (hkl)[1]:

$$\min_{\{A^{(hkl)}\}} \left\{ G_{\text{bulk}} + \sum_{(hkl)} \gamma_{(hkl)} A^{(hkl)} \right\},$$

where $\gamma_{(hkl)}$is the surface energy of the (hkl) facet and $A^{(hkl)}$ is the area of that facet. For isotropic materials—such as liquids—where $\nabla_{\mathbf{n}}\gamma(\mathbf{n}) = \mathbf{o}$, the minimization problem reduces to finding the shape with the minimal surface-to-volume ratio, namely, a sphere.

1.5.1 Anisotropy in Crystalline Solids

In solid crystals, the surface energy varies with crystallographic orientation due to variations in atomic coordination and bond-breaking penalties. For instance, *close-packed planes* (e.g., (111) in FCC metals) have lower γ because of high atomic density and minimal broken bonds. In contrast, *open planes* (e.g., (110)) display higher γ due to undercoordinated surface atoms.

This anisotropy has been confirmed experimentally by cleavage experiments (Tasker, 1979 [Tas79]) and through computational studies (Vitos et al., 1998 [Vit+98]), and it underpins the classical view originally formalized by Gibbs (1875) [Gib78] and later discussed in texts such as Thermodynamics of Materials (Swalin, 1972) [Swa72].

1.5.2 Wulff Construction

Wulff (1901) provided a geometric construction for the equilibrium shape by showing that, for each facet (hkl), the distance $d_{(hkl)}$ from the center of the crystal to that facet is proportional to its surface energy [Wul01]:

$$\frac{d_{(hkl)}}{\gamma_{(hkl)}} = \lambda\,,$$

where λ is a constant (related to the Lagrange multiplier enforcing the volume constraint). This relation implies that facets with lower surface energy (e.g., (111)) extend further from the center and thus occupy larger areas, and facets with higher surface energy (e.g., (110)) are either smaller or absent from the equilibrium shape.

[1] Extension of the Gibbs formulation (1875) for the energy minimization)

For example, in FCC metals such as Au and Pt, the equilibrium shape is often a truncated octahedron dominated by (111) and (100) facets (Baletto & Ferrando, 2005 [BF05]). Wulff's theorem and its implications are discussed rigorously by Dobrushin et al. in the book "Wulff construction, A global shape from local interaction" (1951) [DKW92].

Crystal symmetry also plays a crucial role. In cubic systems, symmetry-equivalent facets (e.g., (100), (010), and (001)) exhibit identical surface energies, leading them to contribute equally to the equilibrium morphology. This equivalence is a direct consequence of the rotational symmetry inherent in the cubic crystal system and is elaborated upon in works such as Crystallography and Crystal Defects (Kelly & Knowles, 2012 [Ant12]).

2 Results and Remarks

In our study, we first compute the surface tension estimates for Aluminum and Palladium along the (100), (110), (111), and (211) facets using two distinct methodologies: the Dangling Bond Model (DBM) and Density Functional Theory (DFT). The DBM quantifies surface energy based on the number of unsatisfied, or dangling, bonds present at a given facet, offering a straightforward model to estimate surface energetics. In parallel, DFT calculations are conducted both with and without ionic relaxation. Ionic relaxation is the process by which the positions of surface atoms are allowed to adjust from their ideal bulk lattice sites, thereby *minimizing the total energy* of the system and capturing the realistic *reconstruction of the surface*. The computed surface tension values were then compared with theoretical surface energy predictions, providing a cross-validation between our computational approaches and theoretical expectations.

Next, we applied the Wulff construction to determine the equilibrium shape of face-centered cubic (fcc) Palladium. For this purpose, the wulffpack package [RE20] was employed to generate the equilibrium morphology based on the computed surface energies for the (100), (110), (111), and (211) facets. According to Wulff's theorem, the distance from the center of the crystal to a given facet is proportional to its surface energy; hence, facets with lower γ values (such as (111)) extend further and occupy larger areas, while those with higher surface energy (such as (110)) are diminished or even absent in the final shape. This construction not only visualizes the equilibrium form of the crystal but also quantitatively confirms the influence of surface energy anisotropy as discussed in the introduction.

In the second exercise, our focus shifts to Aluminum. We repeated the DFT calculations—including ionic relaxation—for Aluminum surfaces modeled with varying numbers of atomic layers ($N_l \in \{5, 6, 7, 8\}$). The aim of this investigation was to study the dependency of the surface tension on slab thickness. By systematically increasing the number of layers, we assessed how the computed surface energy converges to its

asymptotic value (see eq.1.3), thereby highlighting the importance of adequate slab thickness in accurately capturing surface effects.This exercise elucidates the relationship between computational model dimensions and the reliability of surface energy estimations.

Finally, we visualize the relationship between the system's total energy and the number of layers employed in the Aluminum slab models. An ordinary least squares (OLS) regression analysis was performed on the data, allowing us to extract quantitative estimates for the surface energy $\gamma_{(hkl)}$ of the considered facets. Graphical representations of these analyses demonstrated clear convergence trends, confirming that the system's energy stabilizes as the slab thickness increases, and thus validating the reliability of the DFT-based estimators.

2.1 Theoretical Approach of Surface Energy

the theoretical estimation of surface energy in crystalline materials is based on quantifying the energy penalty associated with breaking bonds when a surface is created. In the dangling bond model (DBM), this penalty is determined by the number of unsatisfied (dangling) bonds per surface atom. For a given facet of a crystal, the surface energy γ is estimated as the energy cost per dangling bond, multiplied by the number of dangling bonds per atom, and normalized by the area per atom at the surface.

For FCC crystals, each bulk atom has a coordination number of $z_b = 12$.

The energy required to break all bonds of an atom (the enthalpy of atomization) is given as 326 kJ/mol for Al and 377 kJ/mol for Pd [JL92]. Converting this value to a per-atom basis using Avogadro's number, we obtain the energy per bond:

$$E_{at}^{\mathrm{Al}} = 326 \times 10^3 \times N_A^{-1} J/mol \approx 5.413 \times 10^{-19} J/atom,$$

and

$$E_{at}^{\mathrm{Pd}} = 377 \times 10^3 \times N_A^{-1} J/mol \approx 6.260 \times 10^{-19} J/atom,$$

which represents the typical energy associated with a dangling bond when normalized by the bulk coordination.

When a surface is formed, the coordination number reduces from z_b to a lower value z, depending on the crystallographic facet. The number of dangling bonds per atom is then $N_{db} \coloneqq z_b - z$.

Dividing the total energy penalty by the surface area per atom gives the surface energy γ (see eq.1.3).

The calculations for specific facets of FCC Aluminum are detailed below (of course similar calculations are conducted for the Palladium and any FCC crystal structure).

- **Al(100)**:
  Surface Coordination Number: $z = 8$
  Dangling Bonds per Atom: $N_{db} = z_b - z = 12 - 8 = 4$

Area per Atom (square lattice): $\frac{a^2}{2}$

With $a^{(\mathrm{Al})} = 4.05$ Å[SW71]

$$A^{(100)} = \frac{4.05^2}{2} \approx 8.20\text{Å}$$

Surface energy:

$$\gamma_{(100)} = \frac{4 \times 5.413 \times 10^{-19} J}{12 \times 8.20\text{Å}} \approx 2.20 \times 10^{-20} J/\text{Å}^2 \equiv 2.20 J/m^2.$$

- **Al(110)**:

  Surface Coordination Number: $z = 7$

  Dangling Bonds per Atom: $N_{db} = z_b - z = 12 - 7 = 5$

  Area per Atom (rectangular unit cell): $\frac{a^2}{\sqrt{2}}$

$$A^{(110)} = \frac{4.05^2}{\sqrt{2}} \approx 11.60\text{Å}$$

  Surface energy:

$$\gamma_{(110)} = \frac{5 \times 5.413 \times 10^{-19} J}{12 \times 11.60\text{Å}} \approx 1.94 \times 10^{-20} J/\text{Å}^2 \equiv 1.94 J/m^2.$$

- **Al(111)**:

  Surface Coordination Number: $z = 9$

  Dangling Bonds per Atom: $N_{db} = z_b - z = 12 - 9 = 3$

  Area per Atom (close-packed, hexagonally arranged plane): $\frac{a^2\sqrt{3}}{4}$

$$A^{(111)} = \frac{4.05^2\sqrt{3}}{4} \approx 7.11\text{Å}$$

  Surface energy:

$$\gamma_{(111)} = \frac{3 \times 5.413 \times 10^{-19} J}{12 \times 7.11\text{Å}} \approx 1.90 \times 10^{-20} J/\text{Å}^2 \equiv 1.90 J/m^2.$$

- **Al(211)**:

  The Al(211) surface is more complex due to the presence of multiple types of surface atoms with different coordination environments.

  Total Dangling Bonds: $N_{db} = 10$ (comprising contributions of 5, 3, and 2 dangling bonds from different atomic sites)

  Area per Atom (stepped structure with several "types" of atoms)[2]: $3 \times a^2 \times \sqrt{6}$

$$A^{(111)} = 3 \times 4.05^2 \times \sqrt{6} \approx 119.41\text{Å}$$

[2] This expression doesn't align with the projected area construction and it will be reconsidered in the next paragraph.

Surface energy:

$$\gamma_{(211)} = \frac{10 \times 5.413 \times 10^{-19} J}{12 \times 119.41 \text{Å}} \approx 0.378 \times 10^{-20} J/\text{Å}^2 \equiv 0.38 J/m^2.$$

The calculated theoretical surface energies indicate that the most stable surface (i.e., the one with the lowest surface energy) is Al(111), followed by Al(100) and Al(110).

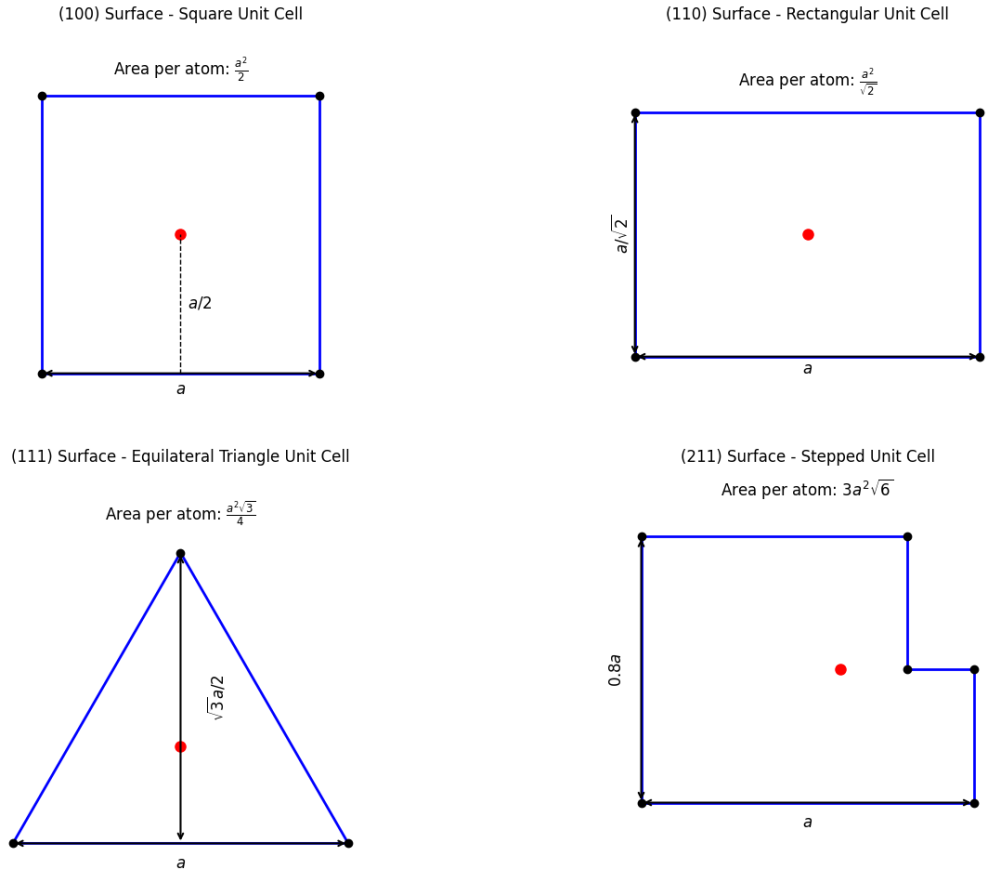

Figure 3: Geometric derivation of the area per surface atom used in estimating the surface energy for each FCC facet. Notice the step-wise ionic configuration in the (211) case, indicating the deficiency of the above contoured surface area implementation in such systems. [plots generated via matplotlib's API.]

2.1.1 Derivation of the Projected Area for FCC (211)

However, the surface energy is defined with respect to the *2D projected area* (i.e. the "footprint" of the surface on a flat plane) rather than the true microscopic area that follows every step and kink. For low-index facets like (100), (110), and (111) the two areas are identical because the surfaces are atomically flat. However, for a high-index surface such as (211) with its stepped structure, the projected area is significantly smaller than the actual contoured area. Using the projected area is the accepted convention in surface science.

Below we briefly explain how to derive the projected area for an FCC (211) surface and then formulate a general expression.

For a cubic lattice with lattice constant a, the plane with Miller indices (h, k, l) intercepts the axes at a/h, a/k, and a/l. For the (211) plane these intercepts are for x-axis: $a/2$ and for y- and z-axis: $a/1$.

A standard way to obtain the projected area of the surface unit cell is to determine two independent vectors that lie in the (211) plane and then compute the area of the parallelogram they span using the cross product. For a cubic system, one can show that the area A_{proj} for a (211) plane is given by

$$A_{\text{proj}}^{(211)} = \frac{3a^2}{\sqrt{6}} \equiv \frac{a^2\sqrt{6}}{2}.$$

To justify this, note that the formula arises from the combination of two factors: First, the denominator $\sqrt{h^2 + k^2 + l^2}$ comes from the normalization of the plane normal; for (211) this is $\sqrt{6}$, and second, the numerator $\sqrt{(hk)^2 + (hl)^2 + (kl)^2}$ for (211) evaluates as $\sqrt{(2 \cdot 1)^2 + (2 \cdot 1)^2 + (1 \cdot 1)^2} = 3$. Thus the projected area is $A_{\text{proj}}^{(211)} \coloneqq \frac{a^2}{\sqrt{6}} \cdot 3 \equiv \frac{a^2\sqrt{6}}{2}$. □

For Aluminum with $a = 4.05$Å, this gives $A^{(211)} = A_{\text{proj}}^{(211)} \approx 20.09$Å, which is the value obtained in the ASE implementation in the DBM. Therefore, we formulate the theoretical values used in benchmarking based on the above formulation, especially for the high-index case, (211), where it yields substantial discrepancies otherwise.

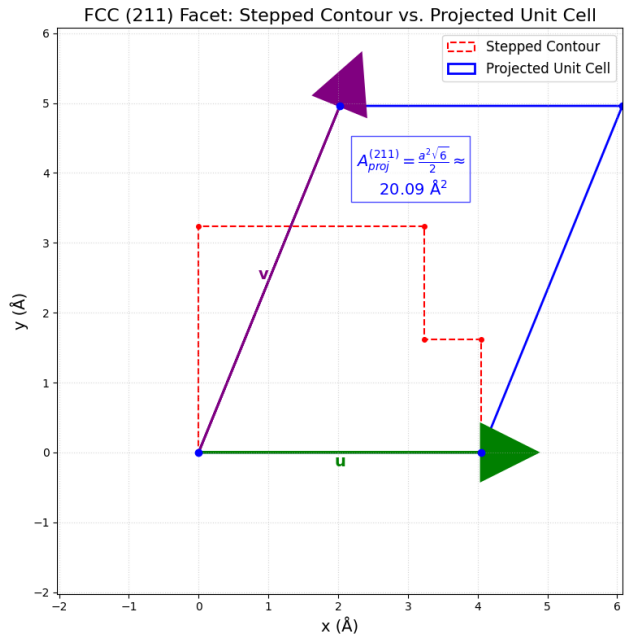

Figure 4: Schematic for the FCC (211) facet. The true stepped (atomic-level) contour is shown in a light dashed outline, while the overlaid solid blue parallelogram represents the 2D projected area with The parallelogram is constructed using two in-plane vectors $\mathbf{u} = (a, 0)$ and $\mathbf{v} = (a/2, a\sqrt{6}/2)$. The two in-plane lattice vectors used to construct the projected unit cell are annotated, and the computed projected area for the Aluminum's case is indicated.[plots generated via matplotlib's API.]

2.2 Comparative Analysis of Palladium and Surface Characteristics

The figure below illustrates how the Pd(211) (and similarly for Al(211)) facet presents a particular arrangement of *under-coordinated atoms* with dangling bonds that can serve as active sites for catalytic reactions[3]. The stepped nature of this high-index facet creates surface atoms with different local environments, which explains its importance in heterogeneous catalysis applications where palladium is commonly used [CA22] (such as in hydrogenation reactions and CO oxidation [Ste+18]).

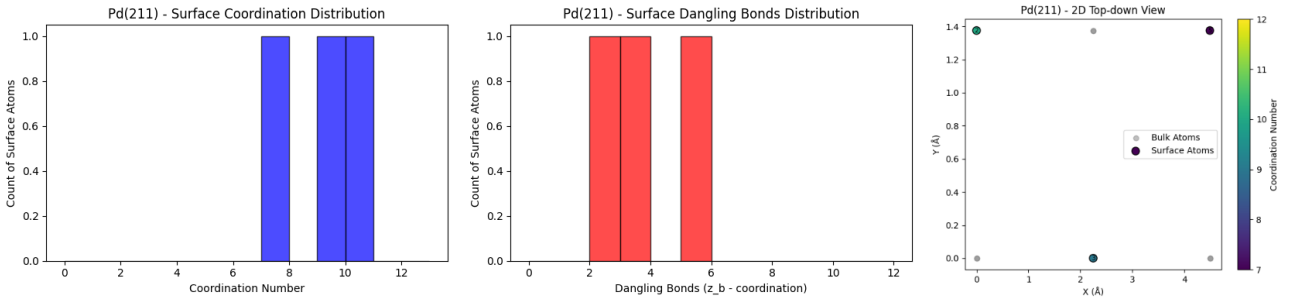

Figure 5: Surface Characterization of Pd(211) Facet. Left: Coordination number distribution showing predominant 8- and 10-coordinated surface atoms. Middle: Dangling bond distribution revealing broken bonds at positions 2-4 and 6. Right: Top-down spatial arrangement of surface (darker) and bulk (gray) atoms, with color scale indicating atomic coordination (7-12).

[3]For the identification of coordination numbers, the `NeighborList` class from `ase.neighborlist` was used with a cutoff distance of 3 Å for both Pd and Al.

Configurational and Computational Set-up on DFT calculations:

slab's size: (1,1,5), except (3,1,5) for (211) facet

k-points: (9,9,1), except (4,9,1) for (211) facet

vacuum: 15 (10 for DBM)

grid spacing: h=0.25

exchange correlation functional: LDA for Al, PBE for Pd

bulk k-points: $(9 \times 9 \times 9)$

bulk symmetry enabled: time reversal, point group

bulk convergence criteria (sufficient successive difference): $E_{\text{bulk}}^{\text{min}} = 10^{-6} eV$, $|n_{\text{min}}| = 10^{-6} eV/\text{Å}^3$

spin polarization: enabled for Pd

relaxation optimizer: BFGS

force tolerance on optimizer: 0.1

maximum iterations on optimizer: 100

Parallelization under MPI protocol: over k-points and domains

available cores used: 8

We also experimented with grid spacing of `h=0.18`, maximum force tolerance of `fmax=0.01` and maximum iterations of `steps=200` for the low-index facets but didn't yield significant improvements on the relaxed structure, especially considering the time overhead.

For the dynamic parallelization configuration implemented on the DFT calculations, we advise the reader to our code implementation `HW_2_codes/utils_DFT.py/` and to `get_parallel_config()` routine, which after obtaining appropriate parallel configuration based on available cores and k-points, it returns a dictionary to pass to GPAW's `parallel` parameter using a simple equipartition split between `kpoints` and `domain` keys of the hashmap to be passed.

Transition metals such as Palladium, possess partially filled d-orbitals. Although bulk Pd is typically considered paramagnetic, the reduced coordination at surfaces or in nanostructured forms can enhance magnetic tendencies by narrowing the d-band and increasing the density of states (DoS) at the Fermi level [Bou+90]. Consequently, even slight exchange splitting can lead to the emergence of local magnetic moments that alter both the electronic structure and the computed surface energies.

For Palladium, the use of the GGA in the form of the PBE functional is a common choice because it tends to provide a balanced description of bonding and magnetic interactions in transition metals. Enabling spin polarization ensures that the calculation can capture any possible magnetic ordering that may occur

due to these d-electron interactions. This is in contrast to Aluminum, a post-transition metal where the electronic structure is dominated by s- and p-orbitals and where magnetism is not expected. Thus, for Al, a spin-unpolarized calculation with a LDA is sufficient.

The following tables summarize the surface energies (in J/m^2) obtained from DFT calculations for different Aluminum and Palladium surfaces, respectively. It shows the values for unrelaxed and relaxed geometries, as well as the absolute differences between them.

- Bulk energies per atom: $E_{\text{bulk}}^{\text{Al}} = -4.140\ eV$, $E_{\text{bulk}}^{\text{Pd}} = -4.587\ eV$.[4]

Table 1: Summary of Surface Energies (J/m²) for Al

Surface	Unrelaxed	Relaxed	Difference
Al(100)	1.01	1.01	0.00 (0.0%)
Al(110)	1.08	1.01	0.07 (6.4%)
Al(111)	1.00	1.00	0.00 (0.0%)
Al(211)	1.03	0.97	0.06 (5.7%)

Table 2: Summary of Surface Energies (J/m²) for Pd

Surface	Unrelaxed	Relaxed	Difference
Pd(100)	4.82	4.78	0.83 (0.8%)
Pd(110)	3.90	3.87	0.08 (7.7%)
Pd(111)	2.54	2.51	0.01 (1.2%)
Pd(211)	5.52	5.17	0.06 (6.3%)

These estimates from unrelaxed and relaxed DFT computations on Pd facets are acceptable considering the ones by Singh-Miller and Marzari [SM09], where although that work focuses more on the relaxed values, it also discusses the "bulk-truncated" (unrelaxed) values.

The table below presents a targeted analysis of the (211) facets. It lists the properties of individual atoms on the surface, including their position (z-coordinate in Å), coordination number, and the number of dangling bonds, along with the total number of dangling bonds calculated.

[4] For `kpts=(12x12x12)`: $E_{\text{bulk}}^{\text{Al}} = -3.713\ eV$, for `kpts=(9x9x9)` and `xc="PBE"`: $E_{\text{bulk}}^{\text{Al}} = -3.685\ eV$.

Table 3: Detailed Analysis of the Al(211) Surface

Atom	z (Å)	Coordination	Dangling Bonds
0	26.57	7	5
1	25.75	9	3
2	24.92	10	2
	Total Dangling Bonds		10

Table 4: Detailed Analysis of the Pd(211) Surface

Atom	z (Å)	Coordination	Dangling Bonds
0	21.12	7	5
1	20.32	9	3
2	19.53	10	2
	Total Dangling Bonds		10

Finally, the below table compares the surface energy values obtained from DFT (both unrelaxed and relaxed) with those predicted by the DBM for various Aluminum and Palladium surfaces respectively.

Table 5: Comparison Between DFT and Dangling Bond Model (DBM) Surface Energies for Al

Surface	DFT Unrelaxed (J/m^2)	DFT Relaxed (J/m^2)	DBM (J/m^2)
Al(100)	1.01	1.01	2.20
Al(110)	1.08	1.01	1.94
Al(111)	1.00	1.00	1.91
Al(211)	1.03	0.97	2.25

Table 6: Comparison Between DFT and Dangling Bond Model (DBM) Surface Energies for Pd

Surface	DFT Unrelaxed (J/m^2)	DFT Relaxed (J/m^2)	DBM (J/m^2)
Pd(100)	4.82	4.78	2.76
Pd(110)	3.90	3.87	2.44
Pd(111)	2.54	2.51	2.39
Pd(211)	5.52	517	2.81

The DFT-based estimates (both unrelaxed and relaxed) for the Aluminum facets—yielding surface energies around 1.0–1.08 J/m^2—agree much more closely with experimental measurements and advanced theoretical studies than the values predicted by the simple DBM. Experimental studies and detailed DFT investigations typically report Aluminum surface energies in the range of approximately 1.0–1.2 J/m^2 for the

close-packed facets (e.g., Al(111)). For example, Vitos et al., reported calculated surface energies for Al of 1.03-1.16 J/m² using FCD-LMTO method [Vit+98].

In contrast, the DBM overestimates the surface energies (for example, predicting 2.20 J/m² for Al(100)), as it does not account for electronic structure effects and the energetic lowering due to ionic relaxation.

The DFT Relaxed approach also correctly captures the trend that the close-packed (111) surface has the lowest energy, followed by (100) and (110), which is consistent with the expected stability ordering of FCC metal surfaces from crystallographic considerations and numerous literature reports.

The illustration below shows a top-down view ((10°, 10°, 0°) rotated) of a Pd(211) surface structure with magnetic moment values displayed on each atom. The visualization represents the atoms as blue circles arranged in the characteristic stepped pattern of a (211) facet.

Each atom displays a numerical value representing its local magnetic moment. These values range from approximately -3.89 to $+0.95 \times 10^{-9} \mu_B$ (Bohr magneton). The presence of both positive and negative values indicates different spin orientations throughout the structure.

Spin polarization is considered for palladium but not for aluminum due to Pd's electronic structure. Palladium ($4d^{10}$) sits near the threshold of ferromagnetism with a high density of states at the Fermi level and strong exchange interactions. This makes Pd susceptible to spin polarization, especially at surfaces where reduced coordination can enhance magnetic effects. In contrast, Al has simple s-p electron configurations with low DoS at the Fermi level, making magnetic effects negligible (as we previously discussed).

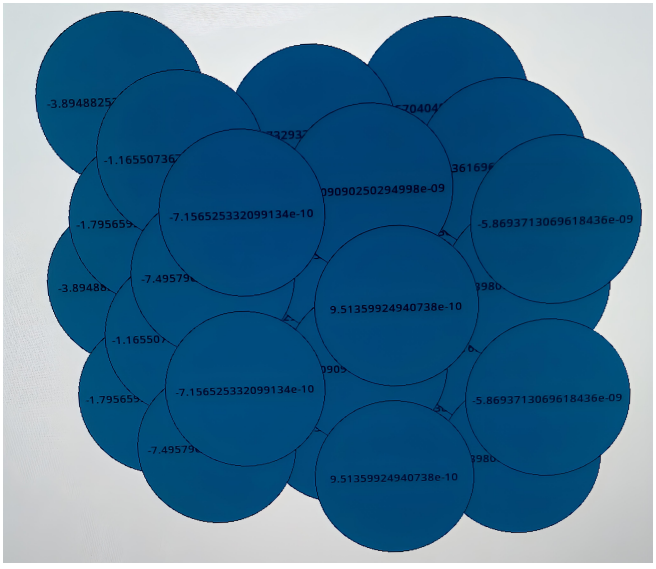

Figure 6: Magnetic moment distribution on Pd(211) surface. The blue circles represent Pd atoms with their calculated local magnetic moments (in Bohr magnetons). The small positive and negative values illustrate the weak spin polarization effects that emerge in Pd surface structures due to its near-ferromagnetic electronic configuration, in contrast to simple metals like Al where spin polarization is negligible.[generated using ASE's API.]

2.2.1 Comparison of Surface Energies

The comparison of surface energies between aluminum (Al) and palladium (Pd) reveals that Pd consistently exhibits higher surface energy values across various facets. For Al, fully relaxed DFT calculations yield surface energies approximately equal to 1 J/m^2 for the (100), (110), and (111) facets, with the (211) facet slightly lower at 0.97 J/m^2. In contrast, our results and literature reports for Pd indicate higher relaxed surface energies.

This disparity arises from fundamental differences in the electronic structures and bonding characteristics of the two metals. Aluminum's bonding is characterized by *delocalized*, nearly free-electron behavior, resulting in relatively *lower cohesive and surface energies*. Palladium, a transition metal, possesses *partially filled d-bands* that lead to more *localized* and directional bonding interactions. These stronger cohesive forces in Pd manifest as higher surface energies, as more energy is required to create new surfaces by breaking these robust bonds.

2.2.2 Wulff Construction of Palladium nanoparticles

The figure below shows a three-panel visualization of palladium nanoparticles (Wulff constructions) at different scales and representations considering the (most accurate) relaxed DFT surface energy estimates of Pd.

Together, these images demonstrate the progression from a theoretical crystal shape model (Wulff construction) to its practical implementation in small (~10 atoms) and large (~500 atoms) palladium nanoclusters, illustrating how theoretical crystal models translate to atomic-scale structures at different sizes.[5]

The ordering $Pd(111) \rightarrow 2.51\ J/m^2$ (lowest) to $Pd(211) \rightarrow 5.17\ J/m^2$ (highest) naturally leads to a shape dominated by the (111) facets, with smaller areas of (110) and (100), and possibly even smaller (or absent) (211) facets in the final polyhedron. The generated Wulff construction should reflect exactly this ratio: the lower the surface energy, the larger (in area) the corresponding facet in the final equilibrium shape.

We can confirm the above discussion in the reference book by Tyson & Miller that gives experimental estimates for various metals, including Pd [TM77].

[5] For the equilibrium shape configuration we used the Science Hub for Atomic-scale Research at Chalmers (SHARC) website.

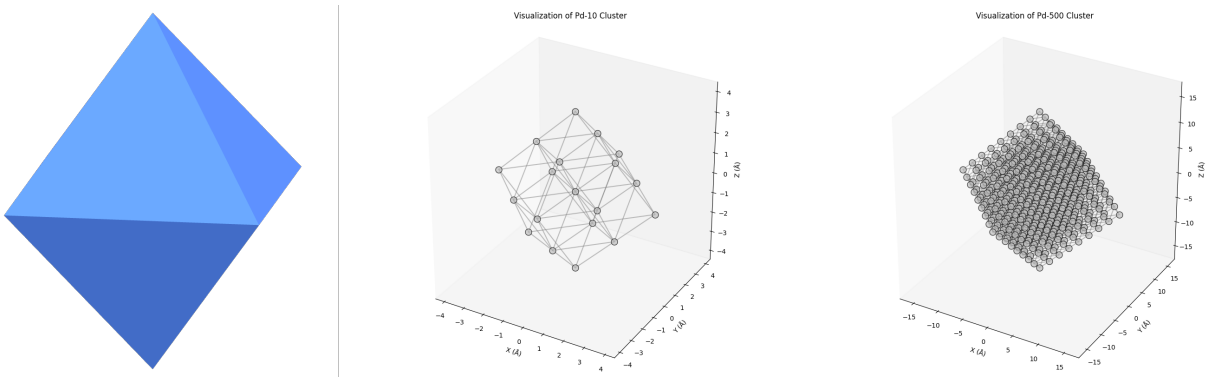

Figure 7: Multi-scale visualization of palladium clusters. Left: SHARC application's Wulff construction UI showing the selected *truncated octahedron* shape with colored facets. Middle: Pd-10 cluster visualization created with ASE and Matplotlib, converted from SHARC output to XYZ format. Right: Larger Pd-500 cluster maintaining the truncated octahedral structure, also visualized using ASE/Matplotlib from SHARC-generated coordinates.

2.3 Convergence Analysis of Surface Energy with Slab Thickness in Aluminum Surfaces

In this part we investigate the convergence of surface energy calculations with respect to slab thickness for aluminum surfaces via DFT calculations. By systematically varying the number of atomic layers and analyzing how surface energy converges, we aim to determine the minimum slab thickness required for accurate surface energy predictions.

In our implementation, we expanded beyond the basic exercise requirements by performing a detailed analysis of both energetic and structural properties. We varied the number of layers uni-axially (i.e., only in the z-direction) while keeping the in-plane dimensions fixed. Specifically, we used supercell sizes of $(1, 1, N_l)$ for low-index facets $\{(100), (110), (111)\}$ and $(3, 1, N_l)$ for the high-index (211) facet, where $N_l \in \{5, 6, 7, 8\}$.

This comprehensive analysis allows one to conclude that while 5-6 layers might be sufficient for qualitative trends, at least 7-8 layers are needed for well-converged surface energies within 0.1 J/m² of the extrapolated infinite-slab limit. The study also revealed the importance of relaxation effects, particularly for the more open surfaces, and demonstrated the systematic discrepancy between simple bond-counting models and first-principles calculations.

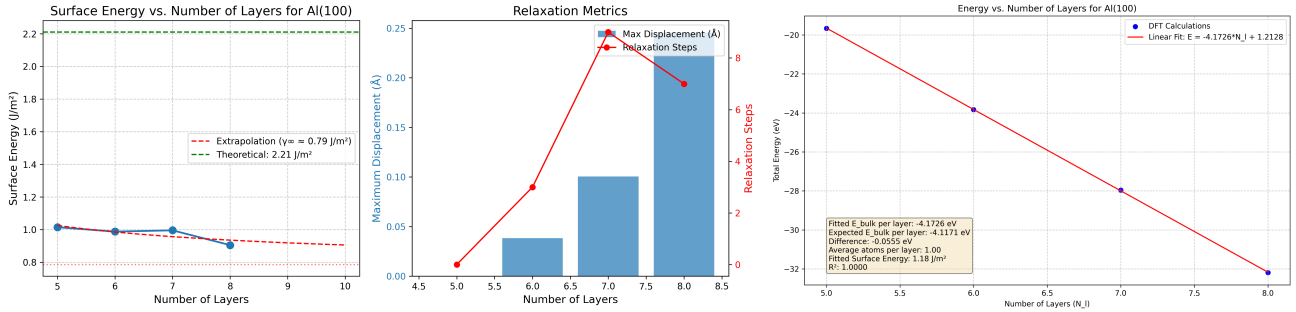

Figure 8: Analysis of Al(100) Surface Properties as a Function of Slab Thickness. Left panel: Surface energy convergence with increasing layers (5-8), showing calculated DFT values (blue dots), extrapolation to infinite thickness (red dashed line, $\gamma_\infty \approx 0.79\ J/m^2$), and theoretical DBM value (green dashed line, $2.21\ J/m^2$). Middle panel: Relaxation metrics displaying maximum atomic displacement (blue bars) and number of relaxation steps (red line) required for convergence at different thicknesses. Right panel: Linear relationship between total energy and number of layers following $E = -4.1726 N_l + 1.2128\ eV$, yielding a surface energy of $1.18\ J/m^2$ and perfect fit ($R^2 = 1$).

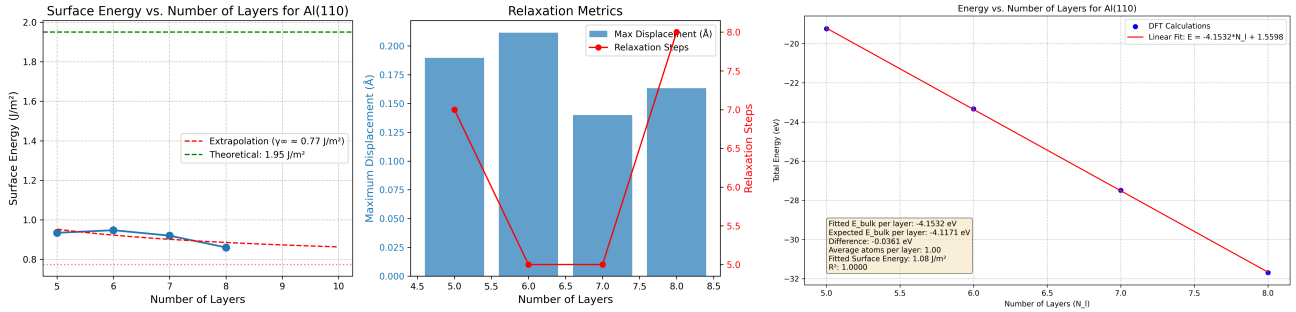

Figure 9: Surface properties of Al(110) as a function of slab thickness. Left: Surface energy convergence (5-8 layers) showing DFT values, extrapolation to infinite thickness ($\gamma_\infty \approx 0.77\ J/m^2$), and theoretical value ($1.95\ J/m^2$). Middle: Maximum atomic displacement and relaxation steps required for convergence. Right: Linear relationship between total energy and number of layers ($E = -4.1532 N_l + 1.5598\ eV$), yielding a surface energy of $1.08\ J/m^2$ ($R^2 = 1$).

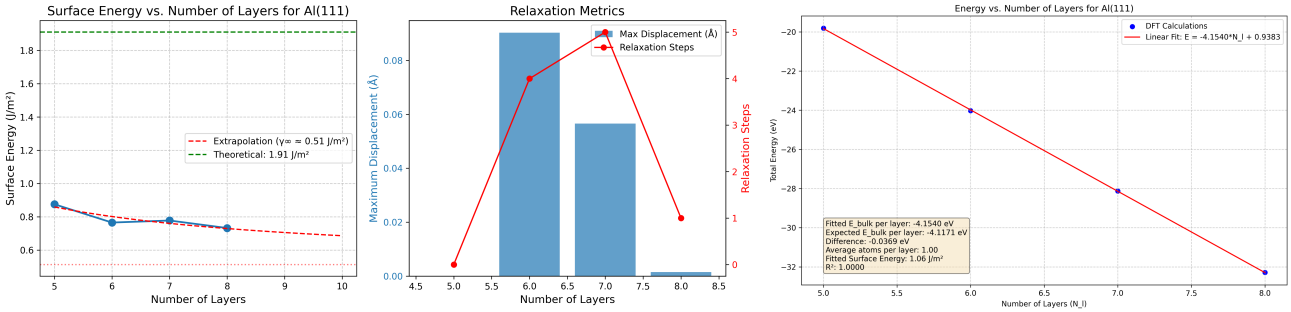

Figure 10: Surface properties of Al(111) as a function of slab thickness. Left: Surface energy convergence (5-8 layers) showing DFT values, extrapolation to infinite thickness ($\gamma_\infty \approx 0.51\ J/m^2$), and theoretical value ($1.91\ J/m^2$). Middle: Maximum atomic displacement and relaxation steps required for convergence. Right: Linear relationship between total energy and number of layers ($E = -4.1540 N_l + 0.9383\ eV$), yielding a surface energy of $1.00\ J/m^2$ ($R^2 = 1$).

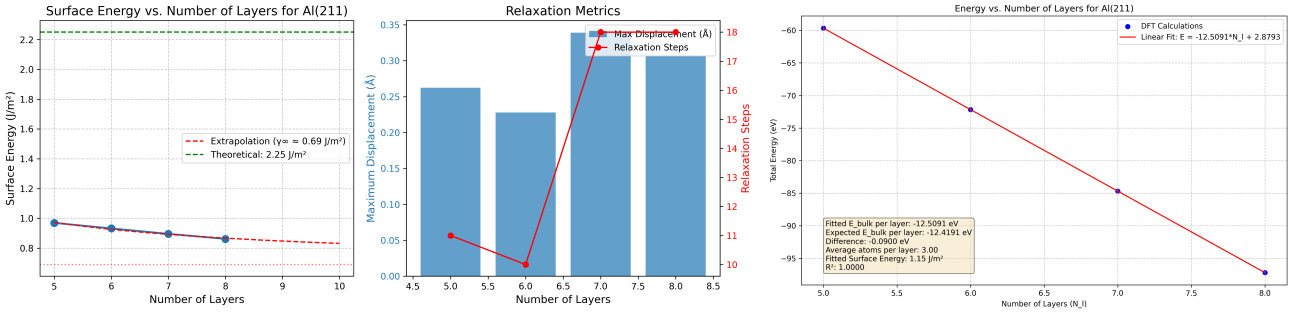

Figure 11: Surface properties of Al(211) as a function of slab thickness. Left: Surface energy convergence (5-8 layers) showing DFT values, extrapolation to infinite thickness ($\gamma_\infty \approx 0.69\ J/m^2$), and theoretical value ($2.25\ J/m^2$). Middle: Maximum atomic displacement and relaxation steps required for convergence. Right: Linear relationship between total energy and number of layers ($E = -12.5091 N_l + 2.8793\ eV$), yielding a surface energy of $1.15\ J/m^2$ ($R^2 = 1$).

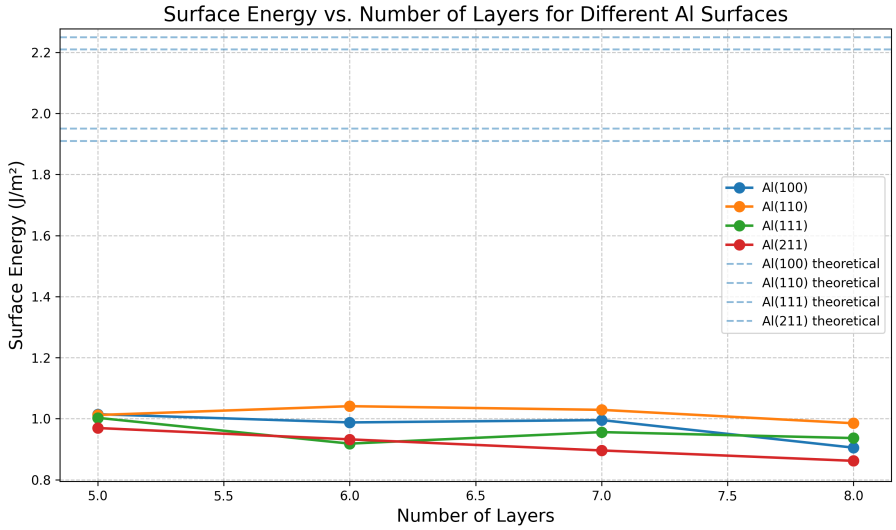

Figure 12: Comparison of surface energy convergence with increasing slab thickness for different aluminum facets: Al(100), Al(110), Al(111), and Al(211). Solid lines represent DFT-calculated values while dashed lines indicate theoretical predictions from the DBM. All facets show decreasing surface energy with increasing layer count, with the (211) facet exhibiting the most significant reduction.

Based on the above experiments, several key insights emerge. The analysis invokes the asymptotic equation provided in the introduction section (eq.1.3), which justifies the extrapolation to infinite layers seen in the left panels of our figures.

All aluminum surfaces show significantly lower calculated surface energies compared to their theoretical values, as clearly demonstrated in the above summary graph. For example, Surface energies range between $0.85 - 1.05\ J/m^2$ for all facets, far below the theoretical values shown by the dashed lines at approximately $1.9 - 2.2\ J/m^2$. The last figure (fig.12) confirms that Al(110) exhibits the highest surface energy ($\sim 0.98 - 1.05\ J/m^2$), followed by Al(100) ($\sim 0.9 - 1.0\ J/m^2$), while Al(111) and Al(211) surfaces have the lowest energies ($\sim 0.85 - 0.95\ J/m^2$). This aligns with the expected stability order for FCC metals where close-packed (111) surfaces are most stable.

The relaxation behavior, depicted in the middle panels, varies significantly between facets. Al(111) shows highest displacement at 6 layers with variable relaxation steps, Al(110) demonstrates inconsistent relaxation patterns with peaks at 6 and 8 layers, and Al(100) shows increasing atomic displacement with thickness. The number of relaxation steps needed for convergence varies non-monotonically with slab thickness, suggesting that computational efficiency is not simply related to model size.

The perfect linear relationships ($R^2 = 1.0$) between total energy and number of layers follow from the surface energy estimate discussed in eq 1.4 of the introduction. This relationship yields fitted bulk energy per layer values that are remarkably consistent across all facets ($\sim 4.153 - 4.173\ eV$), with slight deviations from the expected value ($4.1171\ eV$). When derived from these linear fits, surface energies for Al(100), Al(110), and

Al(111) are 1.18 J/m^2, 1.08 J/m^2, and 1.09 J/m^2 respectively, higher than the extrapolated values but still below theoretical predictions.

This analysis demonstrates the importance of slab thickness in DFT calculations of surface properties and highlights significant discrepancies between calculated and theoretical values that must be considered when modeling aluminum surfaces for applications.

3

Environment Setup

This reference guide specifies user-dependent components of Python codes for performing Density Functional Theory (DFT) calculations using the GPAW (Grid-based Projector Augmented Wave method) software package.

The codes are organized in the directory `HW_2_codes` after tag.gz compression. The sub-directories address various computational results including plots, json and pickle files and trajectory files (in `HW_2_codes/surface_results/`). `HW_2_codes/wulff_constructions_Pd/` directory contains the xyz files for the reproduction of Wulff constructions using the `wulff_cluster_Pd.py` module. In general, one can reproduce and verify the validity of the experiments across the report, given the appropriate resources for manageable execution time.

Remark 3.1. Codes on modules `surface_DFT.py` and `utils_DFT.py` require a proper GPAW (and thus ASE) environment setup. The other modules require only the ASE to be installed. Before running any calculation, users must modify the path settings to match their local installation.

The following code block appears in all scripts of the aforementioned sub-directories and requires user-specific modifications:

```
# Suppress detailed GPAW output
os.environ['GPAW_VERBOSE'] = 'o'
sys.stdout = open(os.devnull, 'w')  # Redirect standard output

# Clear existing paths and set the new one [user-dependent]
intended_path = os.path.expanduser("~/Desktop/DFT_codes/gpaw_datasets"
"/gpaw-setups-0.9.20000")
setup_paths[:] = [intended_path]  # Replace all existing paths
os.environ['GPAW_SETUP_PATH'] = intended_path

sys.stdout = sys.__stdout__  # Restore standard output
print("GPAW looking for datasets in:", setup_paths)
print("Environment GPAW_SETUP_PATH:", os.environ['GPAW_SETUP_PATH'])
```

3.1 Adjusting the Path Settings

Users must update the `intended_path` variable to match their local GPAW dataset installation:

1. Locate your GPAW setups directory (typically installed with GPAW or downloaded separately)
2. Replace `'~/Desktop/DFT_codes/gpaw_datasets/gpaw-setups-0.9.20000'` with the path to your setups directory
3. Ensure the path format is appropriate for your operating system:
    - Linux/macOS: Use `'/path/to/gpaw-setups'` .
    - Windows: Use `'C:/path/to/gpaw-setups'` or `r'C:\path\to\gpaw-setups'` .

References

[Gib78] Josiah Willard Gibbs. "On the equilibrium of heterogeneous substances". In: *American Journal of Science and Arts* s3-16 (1878), pp. 441–458. URL: https://api.semanticscholar.org/CorpusID:130779399.

[Wul01] Georg Wulff. "XXV. Zur Frage der Geschwindigkeit des Wachsthums und der Auflösung der Krystallflächen". In: *Zeitschrift für Kristallographie - Crystalline Materials* 34 (1901), pp. 449–530. URL: https://api.semanticscholar.org/CorpusID:101957155.

[DD63] B. N. Dutta and B. Dayal. "Lattice Constants and Thermal Expansion of Palladium and Tungsten up to 878 °C by X-Ray Method". In: *physica status solidi (b)* 3.12 (1963), pp. 2253–2259. DOI: https://doi.org/10.1002/pssb.19630031207. eprint: https://onlinelibrary.wiley.com/doi/pdf/10.1002/pssb.19630031207. URL: https://onlinelibrary.wiley.com/doi/abs/10.1002/pssb.19630031207.

[HB71] V. Hoffstein and D. S. Boudreaux. "Calculated Low-Energy Electron-Diffraction Intensities for (111) and (110) Surface of Al". In: *Phys. Rev. B* 3 (8 Apr. 1971), pp. 2447–2452. DOI: 10.1103/PhysRevB.3.2447. URL: https://link.aps.org/doi/10.1103/PhysRevB.3.2447.

[SW71] M. E. Straumanis and C. L. Woodward. "Lattice parameters and thermal expansion coefficients of Al, Ag and Mo at low temperatures. Comparison with dilatometric data". In: *Acta Crystallographica Section A* 27.6 (1971), pp. 549–551. DOI: https://doi.org/10.1107/S0567739471001220. eprint: https://onlinelibrary.wiley.com/doi/pdf/10.1107/S0567739471001220. URL: https://onlinelibrary.wiley.com/doi/abs/10.1107/S0567739471001220.

[Swa72] R.A. Swalin. *Thermodynamics of Solids*. A Wiley-Interscience publication. Wiley, 1972. ISBN: 9780471838548. URL: https://books.google.gr/books?id=E_KHeqwctTQC.

[TM77] W.R. Tyson and W.A. Miller. "Surface free energies of solid metals: Estimation from liquid surface tension measurements". In: *Surface Science* 62.1 (1977), pp. 267–276. ISSN: 0039-6028. DOI: https://doi.org/10.1016/0039-6028(77)90442-3. URL: https://www.sciencedirect.com/science/article/pii/0039602877904423.

[Tas79] Philip W. Tasker. "The stability of ionic crystal surfaces". In: *Journal of Physics C: Solid State Physics* 12 (1979), pp. 4977–4984. URL: https://api.semanticscholar.org/CorpusID:120222178.

[Bin+83] G. Binnig et al. "7 × 7 Reconstruction on Si(111) Resolved in Real Space". In: *Phys. Rev. Lett.* 50 (2 Jan. 1983), pp. 120–123. DOI: 10.1103/PhysRevLett.50.120. URL: https://link.aps.org/doi/10.1103/PhysRevLett.50.120.

[Bou+90] S Bouarab et al. "Onset of magnetism in palladium slabs". In: *Physics Letters A* 151.1-2 (1990), pp. 103–105.

[Ing90] John Inglesfield. "Electronic Structure of Metal Surfaces". In: Jan. 1990, pp. 117–153. ISBN: 978-1-4684-8779-4. DOI: 10.1007/978-1-4684-8777-0_5.

[Lan90] M. Lannoo. "The role of dangling bonds in the properties of surfaces and interfaces of semiconductors". In: *Revue de Physique Appliquée* 25.9 (1990), pp. 887–894. DOI: 10.1051/rphysap:01990002509088700. URL: https://hal.science/jpa-00246252.

[DKW92] R Dobrushin, R Kotec, and W. "Wulff construction, A global shape from local interaction". In: (Jan. 1992).

[JL92] A.M. James and M.P. Lord. *Macmillan's Chemical and Physical Data*. Macmillan, 1992. isbn: 9780333511671. url: https://books.google.gr/books?id=J386AQAAIAAJ.

[Boe94] J. C. Boettger. "Nonconvergence of surface energies obtained from thin-film calculations". In: *Phys. Rev. B* 49 (23 June 1994), pp. 16798–16800. doi: 10.1103/PhysRevB.49.16798. url: https://link.aps.org/doi/10.1103/PhysRevB.49.16798.

[FM96] Vincenzo Fiorentini and M. Methfessel. "Extracting convergent surface energies from slab calculations". In: *Journal of Physics Condensed Matter* 8 (Oct. 1996). doi: 10.1088/0953-8984/8/36/005.

[Vit+98] L. Vitos et al. "The surface energy of metals". In: *Surface Science* 411.1 (1998), pp. 186–202. issn: 0039-6028. doi: https://doi.org/10.1016/S0039-6028(98)00363-X. url: https://www.sciencedirect.com/science/article/pii/S003960289800363X.

[ES99] Matthias Ernzerhof and Gustavo E. Scuseria. "Assessment of the Perdew–Burke–Ernzerhof exchange-correlation functional". In: *The Journal of Chemical Physics* 110.11 (Mar. 1999), pp. 5029–5036. issn: 0021-9606. doi: 10.1063/1.478401. eprint: https://pubs.aip.org/aip/jcp/article-pdf/110/11/5029/19111374/5029_1_online.pdf. url: https://doi.org/10.1063/1.478401.

[GS02] Craig A. Gerken and Gabor A. Somorjai. "Low-Energy Electron Diffraction". In: *Characterization of Materials*. John Wiley Sons, Ltd, 2002. isbn: 9780471266969. doi: https://doi.org/10.1002/0471266965.com085. eprint: https://onlinelibrary.wiley.com/doi/pdf/10.1002/0471266965.com085. url: https://onlinelibrary.wiley.com/doi/abs/10.1002/0471266965.com085.

[BF05] Francesca Baletto and Riccardo Ferrando. "Structural properties of nanoclusters: Energetic, thermodynamic, and kinetic effects". In: *Rev. Mod. Phys.* 77 (1 May 2005), pp. 371–423. doi: 10.1103/RevModPhys.77.371. url: https://link.aps.org/doi/10.1103/RevModPhys.77.371.

[SM09] Nicholas E. Singh-Miller and Nicola Marzari. "Surface energies, work functions, and surface relaxations of low-index metallic surfaces from first principles". In: *Phys. Rev. B* 80 (23 Dec. 2009), p. 235407. doi: 10.1103/PhysRevB.80.235407. url: https://link.aps.org/doi/10.1103/PhysRevB.80.235407.

[SS11] D.S. Sholl and J.A. Steckel. *Density Functional Theory: A Practical Introduction*. Wiley, 2011. isbn: 9781118211045. url: https://books.google.gr/books?id=_f994dmAdv0C.

[Ant12] Kevin M. Knowles Anthony Kelly. "Crystal Structures". In: *Crystallography and Crystal Defects*. John Wiley Sons, Ltd, 2012. Chap. 3, pp. 85–122. isbn: 9781119961468. doi: https://doi.org/10.1002/9781119961468.ch3. eprint: https://onlinelibrary.wiley.com/doi/pdf/10.1002/9781119961468.ch3. url: https://onlinelibrary.wiley.com/doi/abs/10.1002/9781119961468.ch3.

[VT12] Michael A Van Hove and Shuk Yin Tong. *Surface crystallography by LEED: theory, computation and structural results*. Vol. 2. Springer Science & Business Media, 2012.

[CL13] Heesung Choi and Maeng-Eun Lee. "First-Principles Investigation of the Surface Properties of LiNiO2 as Cathode Material for Lithium-ion Batteries". In: *Journal of the Korean Electrochemical Society* 16 (Aug. 2013). DOI: 10.5229/JKES.2013.16.3.169.

[Jai+13] Anubhav Jain et al. "Commentary: The Materials Project: A materials genome approach to accelerating materials innovation". In: *APL Materials* 1.1 (July 2013), p. 011002. ISSN: 2166-532X. DOI: 10.1063/1.4812323. eprint: https://pubs.aip.org/aip/apm/article-pdf/doi/10.1063/1.4812323/13163869/011002_1_online.pdf. URL: https://doi.org/10.1063/1.4812323.

[Ong+13] Shyue Ping Ong et al. "Python Materials Genomics (pymatgen): A robust, open-source python library for materials analysis". In: *Computational Materials Science* 68 (2013), pp. 314–319. ISSN: 0927-0256. DOI: https://doi.org/10.1016/j.commatsci.2012.10.028. URL: https://www.sciencedirect.com/science/article/pii/S0927025612006295.

[RP13] Jan Reedijk and K. Poeppelmeier. *Comprehensive Inorganic Chemistry II (Second Edition): From Elements to Applications*. Elsevier Science; 2nd edition (December 29, 2006), Aug. 2013, pp. 1–7196.

[Ste+18] Caomhán Stewart et al. "Unraveling the H2 Promotional Effect on Palladium-Catalyzed CO Oxidation Using a Combination of Temporally and Spatially Resolved Investigations". In: *ACS Catalysis* 8.9 (2018), pp. 8255–8262. DOI: 10.1021/acscatal.8b01509. eprint: https://doi.org/10.1021/acscatal.8b01509. URL: https://doi.org/10.1021/acscatal.8b01509.

PMID: 30221029.

[XBN19] Yuchen Xie, Richard Byrd, and Jorge Nocedal. *Analysis of the BFGS Method with Errors*. 2019. arXiv: 1901.09063 [math.OC]. URL: https://arxiv.org/abs/1901.09063.

[RE20] J. Magnus Rahm and Paul Erhart. "WulffPack: A Python package for Wulff constructions". In: *Journal of Open Source Software* 5.45 (2020), p. 1944. DOI: 10.21105/joss.01944. URL: https://doi.org/10.21105/joss.01944.

[Cha+21] Lowik Chanussot et al. "Open Catalyst 2020 (OC20) Dataset and Community Challenges". In: *ACS Catalysis* 11.10 (2021), pp. 6059–6072. DOI: 10.1021/acscatal.0c04525. eprint: https://doi.org/10.1021/acscatal.0c04525. URL: https://doi.org/10.1021/acscatal.0c04525.

[Wan+21] Yunzhe Wang et al. "Rapid generation of optimal generalized Monkhorst-Pack grids". In: *Computational Materials Science* 187 (2021), p. 110100. ISSN: 0927-0256. DOI: https://doi.org/10.1016/j.commatsci.2020.110100. URL: https://www.sciencedirect.com/science/article/pii/S0927025620305917.

[CA22] Victor M. Chernyshev and Valentine P. Ananikov. "Nickel and Palladium Catalysis: Stronger Demand than Ever". In: *ACS Catalysis* 12.2 (2022), pp. 1180–1200. DOI: 10.1021/acscatal.1c04705. eprint: https://doi.org/10.1021/acscatal.1c04705. URL: https://doi.org/10.1021/acscatal.1c04705.

[MV22] Wolfgang Moritz and Michel A. Van Hove. "Basic Elements". In: *Surface Structure Determination by LEED and X-rays*. Cambridge University Press, 2022, pp. 6–56.

[ZAP22] Cheng Zeng, Tuhina Adit Maark, and Andrew A. Peterson. "Strain in Catalysis: Rationalizing Material, Adsorbate, and Site Susceptibilities to Biaxial Lattice Strain". In: *The Journal of Physical Chemistry C* 126.49 (2022), pp. 20892–20902. doi: 10.1021/acs.jpcc.2c07246. eprint: https://doi.org/10.1021/acs.jpcc.2c07246. url: https://doi.org/10.1021/acs.jpcc.2c07246.

[Mer+23] Amil Merchant et al. "Scaling deep learning for materials discovery". In: *Nature* 624.7990 (2023), pp. 80–85. doi: 10.1038/s41586-023-06735-9. url: https://doi.org/10.1038/s41586-023-06735-9.